RESEARCH ARTICLE
doi.org/10.1002/elsa.202100035

ChemistryEurope
European Chemical Societies Publishing

Received: 3 March 2021
Revised: 19 May 2021
Accepted: 26 May 2021

Spectroelectrochemistry and photoelectrochemistry of electrodeposited ZnO nanorods

Cecilia I. Vázquez[1,2] | **Victoria Benavente Llorente**[1,2] | **Franco M. Zanotto**[1,2] | **Ana M. Baruzzi**[1,2] | **Rodrigo A. Iglesias**[1,2]

[1] Departamento de Fisicoquímica, Facultad de Ciencias Químicas, Universidad Nacional de Córdoba, Córdoba, Argentina

[2] Instituto de Investigaciones en Fisicoquímica de Córdoba INFIQC, Consejo Nacional de Investigaciones Científicas y Técnicas CONICET, Córdoba, Argentina

Correspondence
Cecilia I. Vázquez, Departamento de Fisicoquímica, Facultad de Ciencias Químicas, Universidad Nacional de Córdoba, Pabellón Argentina Ala 1 - Piso 2, Ciudad Universitaria, Córdoba, Argentina.
Email: cvazquez@unc.edu.ar

Abstract

The electrodeposition of nanostructured semiconductors with tunable properties is of vital importance to develop optoelectronic devices. In this work, we introduce a novel synthesis protocol involving a multiple pulse electrodeposition nucleation stage combined with conventional potentiostatic ZnO nanorod growth in a nitrate bath. The in-situ nucleation step allowed a higher surface density of ZnO nanorods. The effect of potential and total charge transferred during the nanorod growth was also systematically studied. Besides, spectroelectrochemical properties of different diameter electrodeposited ZnO nanorods were compared. Electrochemical Burstein-Moss shift was observed for the different diameter ZnO nanorods when the potential was modified. Finally, spectroelectrochemical measurements of small diameter (≈60 nm) ZnO nanorods were carried out under different conditions, for example, electrolyte composition and amount of dissolved O_2, to establish how these parameters affect the Burstein-Moss shift.

KEYWORDS
Burstein-Moss shift, electrochemistry, nanorod, spectroelectrochemistry, zinc

1 | INTRODUCTION

Zinc oxide (ZnO) is a natural n-type direct semiconductor, with a bandgap energy (Egap) of 3.37 eV, absorbing in the UV range. ZnO shows high chemical stability, low toxicity, and is an abundant material with a low-production cost.[1] These properties have made of ZnO an attractive material to optoelectronic applications, as part of third-generation solar cells,[2,3] light-emitting diodes,[4–6] UV photodetectors,[7] photosensors,[8,9] and in photoelectrochemical water splitting.[10,11]

The information on the electronic structure of nanostructured semiconductors is of utmost importance for their application in optoelectronic devices. Fitzmaurice et al first applied the in-situ spectroelectrochemical method for the determination of the conduction band edge of TiO_2 porous thin films.[12] This approach was further adapted and developed to the characterization of different electronic properties of nanostructured semiconductors, as trap states within the bandgap,[13] conduction band (CB) unpinning,[14] and vacant electronic states distributed near the CB edge.[15] In a previous report, we presented the spectroelectrochemical properties and photocurrent transients of ZnO nanorods prepared by the hydrothermal method.[16] It was concluded that the dependence of the optical Egap on the nanorod diameter according to the Burstein-Moss

RESEARCH ARTICLE
doi.org/10.1002/elsa.202100035
Chemistry Europe
European Chemical Societies Publishing

shift theory was due to the presence of surface states. Besides, during cathodic polarization in the spectroelectrochemical experiments, an absorbance decrease and Egap shift at different potentials were observed.

Several methods have been used to prepare ZnO nanostructures, for example, vapor deposition,[17] reactive magnetron sputtering,[18] pulsed laser deposition,[19] hydrothermal,[8,16] successive ionic layer adsorption and reaction (SILAR),[20] and electrodeposition.[21] Electrodeposition is fast, simple, and it can be applied to substrates with a large area. Typically, ZnO nanostructures are cathodically electrodeposited from aqueous solutions containing different Zn^{2+} salts by reducing O-containing oxidants, such as dissolved O_2,[22] H_2O_2,[23] or NO_3^- ions.[24,25] In the last case, nitrate ions can be cathodically decomposed, within the potential window, forming interfacial HO^- ions as subproducts that in turn can crystallize with Zn^{2+} ions and slowly grow as a nanoporous ZnO film at the electrode interface.[21,26] With this approach, different ZnO morphologies can be attained, like thin films,[27] nanoflowers,[28] and nanorods[29,30] among others. Particularly, high aspect ratio ZnO nanorods are of importance due to their preferential electron transport along the nanorod axis.[31] Several works have described the electrodeposition of ZnO nanorods from nitrate-containing solutions. In general, a single potential/current pulse is applied in a pre-seeded substrate.[29] The seeds can be deposited on the conductive substrate via a chemical method, like thermal decomposition of zinc acetate[32] or spray pyrolysis[33]; alternatively, the seeds can also be deposited on the surface by electrochemical methods using a two-step electrochemical program.[34–36] Multiple potential pulsed electrodeposition (MPED) has been reported as an effective method to grow different nanostructured ZnO morphologies, in absence of the seeding step.[37,38] During MPED, a sequence of successive short pulses (1 s) is applied alternating between negative overpotentials and the open circuit potential (OCP). The pauses at OCP allow the diffusion of reacting ions, suppressing in this way undesired reaction pathways such as gas formation.[26] Under MPED, it is possible to modify the ions diffusion profile and, the surface morphology of the structures could be controlled. A highly negative overpotential is applied during the seeding step. It generates a high concentration of HO^- ions in a very short time that favors ZnO crystals nucleation over the electrode surface. By switching the potential to a positive enough value, HO^- ion generation is interrupted. The excess generated HO^- ions diffuse away from the interface avoiding a sustained growth of the initial seeds. Repeating the cycle allows for more nucleation events.

The present report aims to improve ZnO nanorods electrodeposition strategies based on pulsed step potential programs in nitrate solutions. Particularly, we use the MPED for the seeding step. Besides, the paper also pursues providing a deeper understanding of the electronic structure of the nanorods via a detailed spectro- and photoelectrochemical characterization.

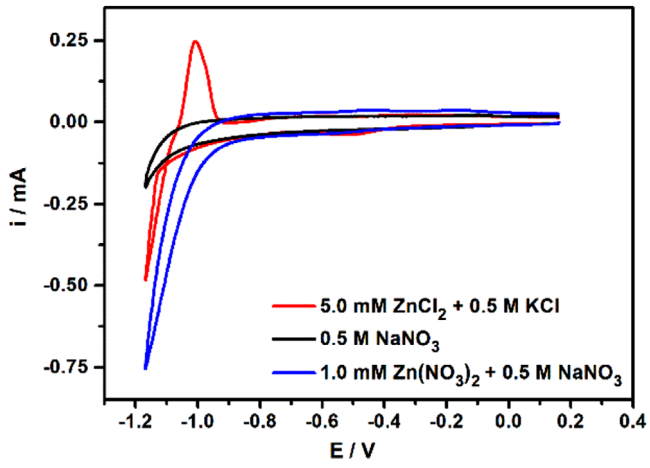

FIGURE 1 Cyclic voltammetric scans of 5.0 mM $ZnCl_2$ + 0.5 M KCl (red curve); 0.5 M $NaNO_3$ (black curve) and 1.0 mM $Zn(NO_3)_2$ + 0.5 M $NaNO_3$ (blue curve). Working electrode: ITO glass. Reference electrode: Ag|AgCl|$KCl_{(aq,sat)}$. Counterelectrode: Pt wire. Sweep potential rate: 200 mV/s. Solutions have the same ionic strength and were previously purged with N_2

2 | RESULTS AND DISCUSSION

2.1 | ZnO electrodeposition onto ITO from NO_3^- solutions

Figure 1 shows the cyclic voltammetry of ITO in different electrolytes. The voltammogram corresponding to $ZnCl_2$ solution (without the addition of NO_3^- ions, red curve) shows the typical profile of Zn^0 electrodeposition onto a foreign substrate[39]: during the cathodic potential sweep there is a negative increase in the current due to Zn^{2+} ions reduction to Zn^0; while on the reverse potential scan, the metallic zinc deposition continues on the previously deposited Zn^0, showing a crossover between forward and backward scan and the characteristic peak for zinc stripping at -1.0 V. On the other hand, when the electrolyte is 0.5 M $NaNO_3$ (without the addition of Zn^{2+} ions, black curve) there is an increase on the cathodic current due to the irreversible NO_3^- reduction, producing NO_2^- and HO^- ions at the electrochemical interphase (Reaction 1).[40] It should be noted that both previous processes occur at similar reduction potential values. When 1.0 mM $Zn(NO_3)_2$ is incorporated into the electrolytic solution (both Zn^{2+} and NO_3^- ions present, blue curve) there is a fourfold increase of the cathodic current starting at a more less cathodic potential, approximately -0.9 V. This cathodic

doi.org/10.1002/elsa.202100035

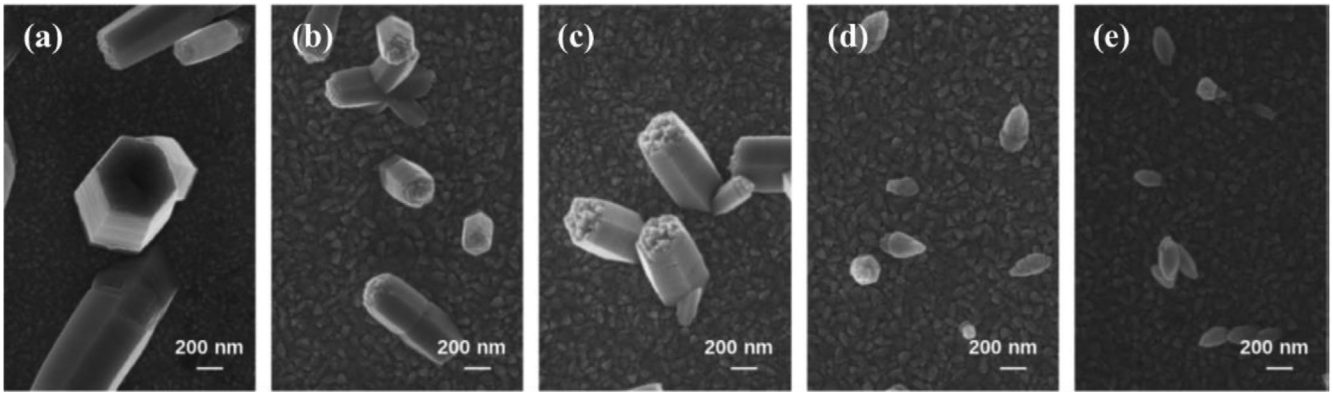

FIGURE 2 SEM images of electrodeposited ZnO nanorods onto ITO at different constant cathodic potentials (Ec) until -200 mC/cm^2 of transferred charge was achieved. The sample name, Ec and ZnO nanorods average diameter are, respectively: (A) *SP1*, -0.80 V, (0.7 ± 0.2) μm; (B) *SP2*, -0.95 V, (0.28 ± 0.05) μm; (C) *SP3*, -1.00 V, (0.35 ± 0.04) μm; (D) *SP4*, -1.12 V, (0.17 ± 0.04) μm, and (E) *SP5*, -1.22 V, (0.11 ± 0.03) μm. The electrolyte solution was 1.0 mM $Zn(NO_3)_2$ + 0.5 M $NaNO_3$ at 80°C

TABLE 1 Sample names, grow potential (Ec) used for the preparation of ZnO nanorods and nanorod average diameter (d) for Single potential pulses samples SP- (with no previous nucleation)

Sample name	***SP1***	***SP2***	***SP3***	***SP4***	***SP5***
Ec (V)	−0.80	−0.95	−1.00	−1.12	−1.22
d (μm)	0.7±0.2	0.28±0.05	0.35±0.09	0.17±0.04	0.11±0.03

current peak is assigned to the reduction of NO_3^- catalyzed by the precipitation of $Zn(HO)_2$ and its spontaneous dehydration to ZnO. This assignment is supported by the absence of the stripping peak mentioned before at -1.0 V, indicating the absence of Zn^0 on the electrode surface. The catalytic effect is due to the coupled precipitation reaction of $Zn(HO)_2$, *i.e.* an electrochemical reaction followed by a chemical reaction with a high equilibrium constant value ($Ks(Zn(HO)_2) = 3.3 \times 10^{16}$).[33,41] Proposed steps are as follows:

$$NO_3^-{}_{(aq)} + H_2O_{(l)} + 2e^- \rightarrow NO_2^-{}_{(aq)} + 2HO^-{}_{(aq)} \quad (1)$$

$$Zn^{2+}{}_{(aq)} + 2HO^-{}_{(aq)} \rightarrow Zn(HO)_{2(aq)} \rightarrow ZnO_{(s)} + H_2O_{(l)} \quad (2)$$

A systematic study on the effect of the applied potential onto the morphology of the electrodeposited ZnO was carried out. For this purpose, a single potential pulse program was used. The potential was stepped from Open Circuit Potential (OCP) to several cathodic potential values (***Ec***) during a given time until -200 mC/cm^2 of transferred charge was attained. The corresponding chronoamperometric profiles are displayed in Figure S1 in the Supporting Information and the SEM images of ZnO electrodeposited nanostructures are shown in Figure 2. In Table 1, the sample names, applied Ec and ZnO nanorod average diameters (d) are summarized.

As the deposition potential is more negative and the current is higher, the deposition process will be different. At more negative potentials there is a higher surface density of ZnO nanorods (see Figure S2) as there is an increase of the ITO nucleation active sites.[42] Samples prepared at -0.80 V are 700 nm diameter hexagonal columns, with typical wurtzite- type structures of ZnO, as can be confirmed by the presence of intense vibrational bands at 110 and 440 cm^{-1} (E2 low and E2 high, respectively) in the Raman spectra[43] and the corresponding peaks in the XRD patterns[16] (see Figure S3). The analysis of SEM images indicates that the more negative the applied potential the smaller the ZnO nanorods; they become pointier, and also lose the hexagonal shape. This behavior can be analyzed by considering the current density transferred during the electrodeposition. The lower current density (at lower overpotentials) implies a decrease in HO^- ion rate generation (Reaction 1), so Zn^{2+} ions diffuse fast enough from the solution bulk to the nanorod lateral faces, increasing its diameter.[37] At high cathodic potentials, the current density is also high, increasing the rate generation of HO^- ions. When the HO^- ions concentration is very high, the interfacial pH increases, and soluble Zn^{2+} species, such as $[Zn(HO)_3]^-$ and $[Zn(HO)_4]^{2-}$, are favored (Reactions 3 and 4) as can be observed in the species distribution diagram of

RESEARCH ARTICLE
doi.org/10.1002/elsa.202100035
Chemistry Europe
European Chemical Societies Publishing

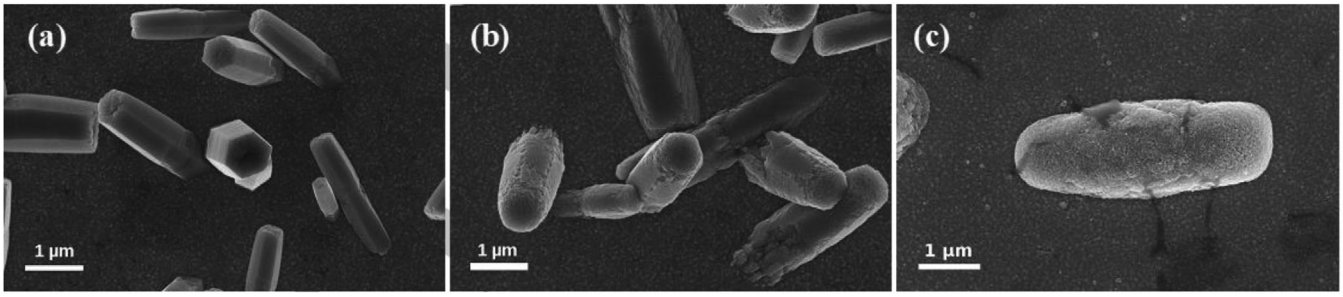

FIGURE 3 SEM images of electrodeposited ZnO nanorods onto ITO at low overpotentials until different values of transferred charge (Q). Q values, Ec and ZnO nanorods average diameter are, respectively: (A) -200 mC/cm^2, -0.80 V, (0.7 ± 0.2) μm; (B) -300 mC/cm^2, -0.80 V, (1.0 ± 0.2) μm, and (C) -567 mC/cm^2, -0.95 V, (2.0 ± 0.3) μm. The electrolyte solution was 1.0 mM $Zn(NO_3)_2$ + 0.5 M $NaNO_3$ at 80°C

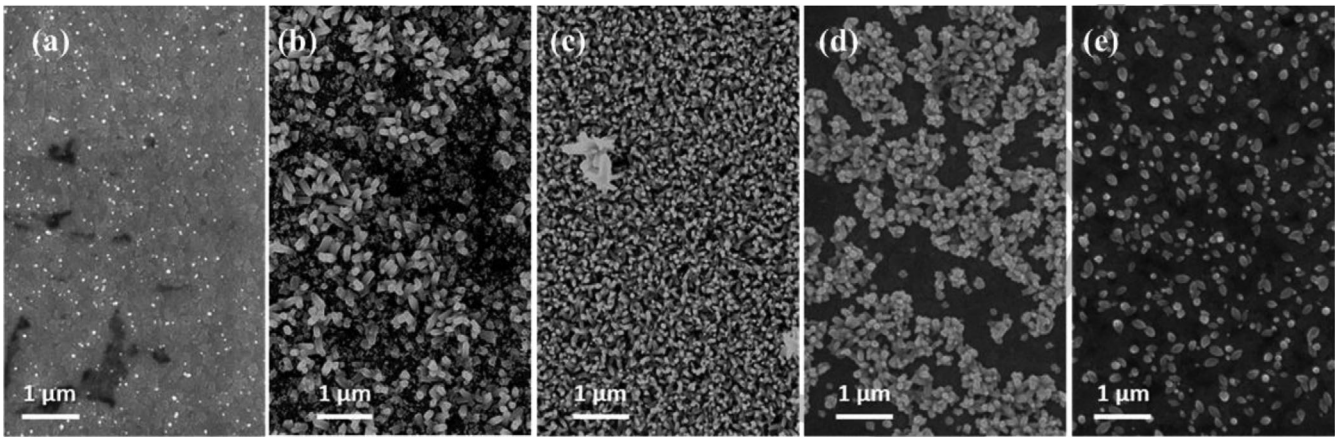

FIGURE 4 (A) SEM images of sample MP0, ZnO nanoparticles onto ITO electrodeposited by 10 seeding cycles with a particle average diameter of (3.2±0.9).10 nm; (B-E) Seeded samples after a growing step at different Ec until reaching -50 mC/cm^2: sample name, Ec and average ZnO nanorod diameter are indicated, respectively: (B) *MP1*, -0.80 V, (11±2).10 nm; (C) *MP2*, -0.90 V, (6±1).10 nm; (D) *MP3*, -1.00 V, (9±2).10 nm, and (E) *MP4*, -1.10 V, (11±2).10 nm. The electrolyte solution was 1.0 mM $Zn(NO_3)_2$ + 0.5 M $NaNO_3$ at 80°C

Zn-species in Figure 4.

$$ZnO_{(s)} + HO^-_{(aq)} + H_2O_{(l)} \rightarrow \left[Zn(HO)_3\right]^-_{(aq)} \quad (3)$$

$$ZnO_{(s)} + 2HO^-_{(aq)} + H_2O_{(l)} \rightarrow \left[Zn(HO)_4\right]^{2-}_{(aq)} \quad (4)$$

Considering this latter aspect, at high pH values, Zn^{2+} soluble species prevail leading to progressive dissolution of $Zn(HO)_2$ (and ZnO) precipitate, thus the ZnO nanostructures dissolve, decreasing their size and showing rougher surfaces. Figure 2 shows the progressive change of size, morphology, and roughness of the ZnO nanoparticles prepared at increasingly negative deposition potentials.

A similar effect in the ZnO nanorod morphology is observed when the transferred charge density during the deposition is high. Figure 3 displays the SEM images of ZnO nanorods deposited at low overpotentials (samples *SP1* at -0.80 V and *SP2* at -0.95 V) during different amounts of time. When the transferred charge is higher, the hexagonal shape of the ZnO nanorods is less noticeable and the rods are larger and more porous, indicating the presence of simultaneous deposition and dissolution processes.

The presented results demonstrate that it is possible to control the shape, size, and quality of the electrodeposited nanorods. However, it was not possible to control the nanorod surface density, that is, the coverage of the electrode with nanorods was not tunable with the previous experimental variables. In order to obtain a higher surface density of ZnO nanorods, a multiple potential pulse program was applied. It consisted of two stages: (a) Seeding: 10 fast pulses of 1.0 s at -1.5 V and 5.0 s at 0.16 V and (b) Growth: a constant pulse at potential ***Ec*** until a charge of -50 mC.cm^{-2} was reached (see Figure 4).

The influence of a larger number of seeding cycles in the sample morphology and the chronoamperometric profiles of the growth stage are displayed in Figures S5 and S6, respectively. In Table 2, the sample names, applied Ec and ZnO nanorod average diameters (d) from SEM images in

RESEARCH ARTICLE
doi.org/10.1002/elsa.202100035
Chemistry Europe
European Chemical Societies Publishing

TABLE 2 Sample names, grow potential (Ec) used for the preparation of ZnO nanorods and nanorod average diameter (d) for Multiple potential pulses samples MP- (with previous MPED nucleation)

Sample name	*MP0*	*MP1*	*MP2*	*MP3*	*MP4*
Ec (V)	—–	−0.80	−0.90	−1.00	−1.10
d (x10nm)	3.2±0.9	11±2	6±1	9±2	11±2

Figure 4 are summarized. In Figure 4A, there is an SEM image of the seeded substrate, consisting of spherical particles of about ~30 nm in diameter, homogeneously distributed over the ITO surface. The off-time at 0.16 V aids in the relaxation and the rearrangement of deposited atoms leading to the possibility of new nucleation sites during the subsequent deposition. In consequence, the nuclei surface density increases, and the deposit uniformity is improved. When the second stage is applied, ZnO nanorods grow upon the seeds with a diameter between 60 and 110 nm, independently of the applied potential. In all samples, the ZnO nanorod surface density is much higher than without the seeding stage, compared with Figure 2 and Figure S2. In Figure 4B-E, as ***Ec*** is more negative, for example, at -1.10 V for sample *MP4*, nanorods progressively lose the hexagonal shape and the ZnO nanorod surface density is lower. As was pointed out before, at more negative potential values the HO^- ions concentration is higher, hence, the ZnO nanorods are partially dissolved, as well as some of the ZnO seeds deposited during Stage 1.

2.2 | Photoelectrochemical measurements

Photoelectrochemical measurements were carried out in 1.0 M $LiClO_4$ solutions, purged with N_2. A potential pulse of 0.8 V was applied while white light was switched on and off and the photocurrent was recorded. The experimental set-up is depicted in Figure 5A. Figure 5B shows the transient photocurrent profiles.

The photocurrent for ITO (black curve) is almost negligible. When the photoanode surface is modified with large ZnO nanorods (sample *SP1* - blue curve), the photocurrent raises almost two orders of magnitude. The fast increase of photocurrent in ITO electrodes modified with ZnO nanorods indicates an efficient separation of charge carriers. The photocurrent increase is even more pronounced when the ZnO synthesis was performed via a multiple pulse potential program as for sample *MP2*, due to the high nanorod surface coverage. Furthermore, the smaller diameter of the *MP2* sample could also contribute to the higher photocurrent observed. The required hole diffusion distance to the semiconductor|electrolyte interface is smaller from a photogenerated electron-hole pair when the diameter is smaller, thus, preventing possible recombination processes, and improving photoelectrochemical performance.[44]

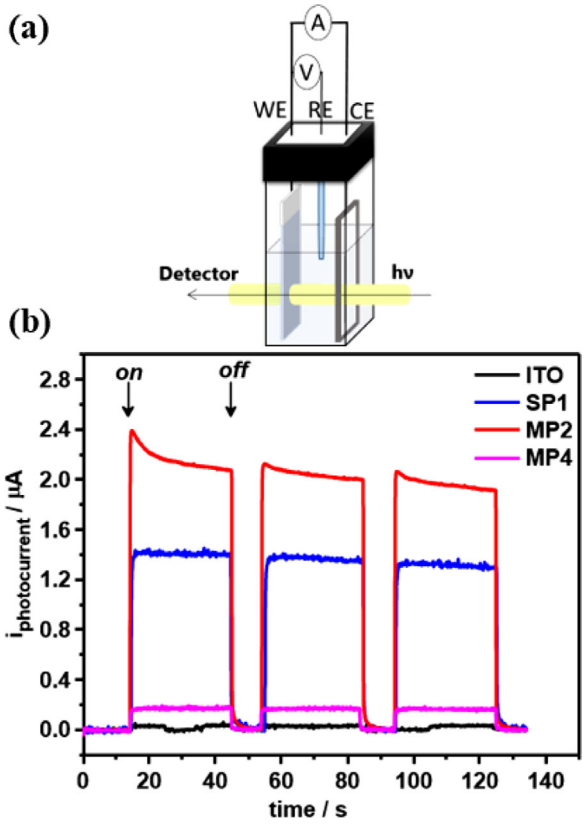

FIGURE 5 (A) Experimental setup for photo and spectroelectrochemical measurements. (B) Photocurrent measurements of different samples at 0.8 V in 1.0 M $LiClO_4$ after N_2 purge

On the other hand, if the deposition potential is too negative, as for sample *MP4*, the nanorod surface density is low and the photocurrent is much lower compared to the other samples. Probably, photogenerated current is quenched by the high electron density from exposed ITO. The photocurrent peak present in high-absorbing samples like *MP2* could be due to mass transport limitation of the hole-scavenger specie from the solution bulk.[45] This feature involves initially an accumulation of holes in the interface due to low rate of transfer of holes to the electrolyte and a subsequent electron-hole recombination in the surface.[46]

In brief, in terms of solar cell photoanode it is better the implementation of MPED nucleation, in order to achieve

RESEARCH ARTICLE
doi.org/10.1002/elsa.202100035
Chemistry Europe
European Chemical Societies Publishing

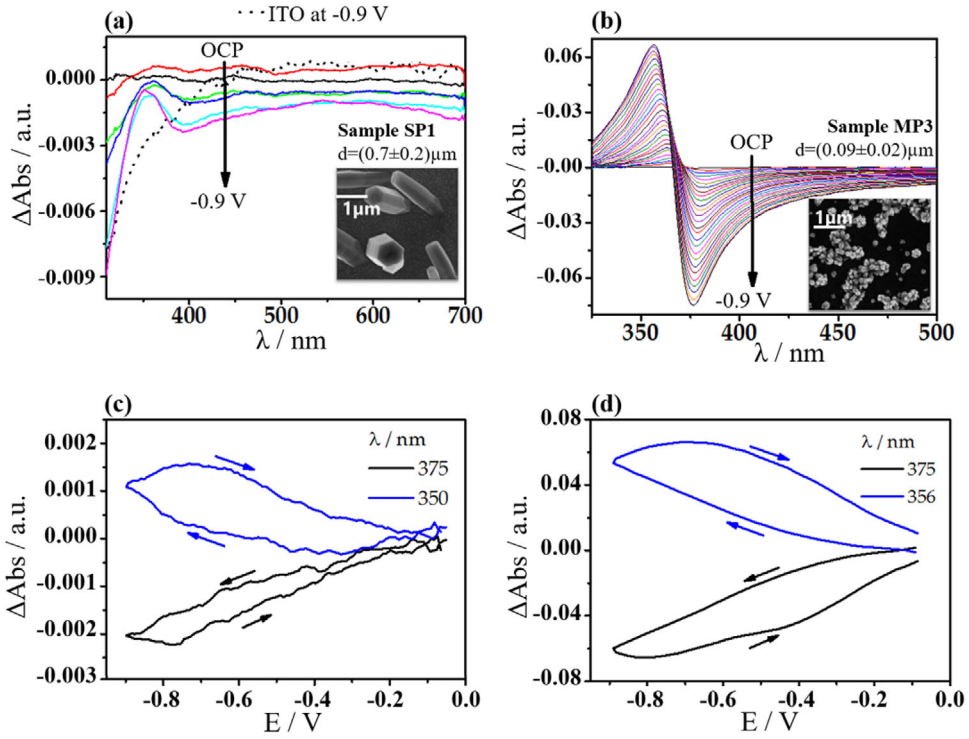

FIGURE 6 Spectral variation of *ΔAbs* at different potential for samples: **(A)** *SP1*, d = (0.7± 0.2) μm and **(B)** *MP3*, d = (0.09 ± 0.02) μm. In the inset there is a SEM image of the sample. **(C)** and **(D)** Variation of ΔAbs at two different wavelengths with applied potential for the samples in **(A)** and **(B)**, respectively. Experimental parameters: 10 mM $LiClO_4$ aqueous solutions, previous purged with N_2; sweep rate: 10 mV/s

larger ZnO nanorod surface density with a not so large grow overpotential, to avoid nuclei and nanorod dissolution.

2.3 | Spectroelectrochemical measurements

The experimental setup is shown in Figure 5A. The ITO|ZnO absorption spectrum was simultaneously acquired with the potentiodynamic scan, performed from OCP down to -0.9 V and back to OCP in 10 mM $LiClO_4$ aqueous solutions. The initial absorption spectrum at OCP was used as the reference spectrum. In this way, the change in the absorbance (*ΔAbs*) versus wavelength (λ) at different potentials was recorded (reference spectrum taken at OCP).

Figure 6A,B displays the spectroelectrochemical results obtained during the cathodic sweep (from OCP to -0.9 V) for samples *SP1* (nanorod diameter, d = (0.7± 0.2) μm, large ZnO nanorods) and *MP3* (d = (0.09 ± 0.02) μm, small ZnO nanorods), respectively. In both samples, there are two different trends in the ZnO nanorod absorption: bleaching at about 375 nm and an increase of absorbance at 350-356 nm. Figures 6C,D shows the dependence of *ΔAbs* values at 375 (black) and 350-356 nm (blue) as a function of the applied potential during the cyclic voltammetry for large and small ZnO nanorods, respectively. During the cathodic sweep, for large ZnO nanorods, *ΔAbs* was appreciable starting at -0.2 V and for small nanorods, right before OCP. In both cases, the bleaching and increase in *ΔAbs* occurred simultaneously with the potential variation and the maximum change was attained at about -0.7 V. During the anodic sweep (from -0.9 V to OCP), the *ΔAbs* was reversed until the initial optical absorbance is completely recovered. It is worth noticing that the absolute values of *ΔAbs* are markedly higher for smaller ZnO nanorods.

The bleaching in the absorbance could be described as an electrochemical Burstein-Moss shift.[16,47] When a negative overpotential is applied to the electrode, the quasi-Fermi level is raised and empty states in the conduction band are populated by injected electrons. If the substrate is illuminated, the optical excitation of electrons from the valence band to those states is now inherited, so the sample absorbance diminishes. It is important to note that *ΔAbs* minimum is found at 375 nm, close to the absorption onset of a direct transition for ZnO (370 nm). Besides, as was pointed out before, the absolute values of *ΔAbs* are markedly higher in smaller ZnO nanorods. It has been reported that the ZnO surface presents defects that produce donor levels, such as O vacancies and interstitials Zn atoms. Usually, oxygen vacancies in ZnO serve as

RESEARCH ARTICLE
doi.org/10.1002/elsa.202100035
Chemistry Europe
European Chemical Societies Publishing

n-type dopants and supply free electrons in the conduction band.[48] As a result, the number of available mid-gap states is proportional to the nanorod area to volume ratio (A/V). Small ZnO nanorods have a high A/V ratio, consequently, a large number of surface defects and trap levels; which in turn are more affected by changes in the cell potential. Therefore, as the potential is swept to more negative values, the electrode quasi-Fermi level is raised and more electrons could be injected into the trap levels, diminishing more markedly the small ZnO nanorods absorbance.

Some semiconductor oxides could present electrochromism due to Li^+ ion intercalation into the crystalline lattice assisted by the applied potential.[49] This is possible for ZnO since Li^+ ion has 59 pm of ionic radius and Zn^{2+}, 60 pm, considering a coordination number of 4.[41] To corroborate that the observed phenomena correspond to a Burstein-Moss shift, spectroelectrochemical experiments where performed in different electrolyte solutions containing 0.1 M Li^+, Na^+, and K^+ ions, which present ionic radii 59, 99, and 137 pm, respectively (Figure 7A). The variation of *ΔAbs* is of the same magnitude and at the same potentials in all three electrolytes, moreover, there is no dependence on *ΔAbs* with the Li^+ ion concentration or different counter ion species (see Figure S7). Hence, the optical changes are not related to Li^+ ion intercalation into the ZnO lattice, and the observed bleaching can be certainly attributed to an electrochemical Burstein-Moss phenomenon. For CdSe quantum dots it was reported a dependence of the Burstein-Moss shift onset potential with the electrolyte cation.[50] However, in our case, the dependence of *ΔAbs* with the potential is not altered when different sized cations and anions are used as electrolytes. This observation indicates that the potential required for electron injection is not limited by the interaction with the image charge in the electrolyte. In addition, spectroelectrochemical experiments were performed in 0.1 M $LiClO_4$ at different sweep rates (Figure 7B). The optical changes were not affected by the potentiodynamic sweep rate, implying that the process is not controlled by diffusion and the *ΔAbs* values depend only on the applied potential (for the same electrode and illumination intensity), that is, on the raise in quasi-Fermi level and on the number of electrons injected into the conduction band.

It is well known that dissolved O_2 can act as an electron scavenger in photocatalytic reactions, so to evaluate the role of oxygen during the development of electrochemical Burstein-Moss shift phenomena, spectroelectrochemical measurements were performed in the absence (or presence) of dissolved O_2 in the electrolyte via purging (or not) the solution with N_2. A constant pulse of -0.9 V was applied to the electrode until a constant *ΔAbs* value was attained; afterward, the current was set to 0 A and the change in the

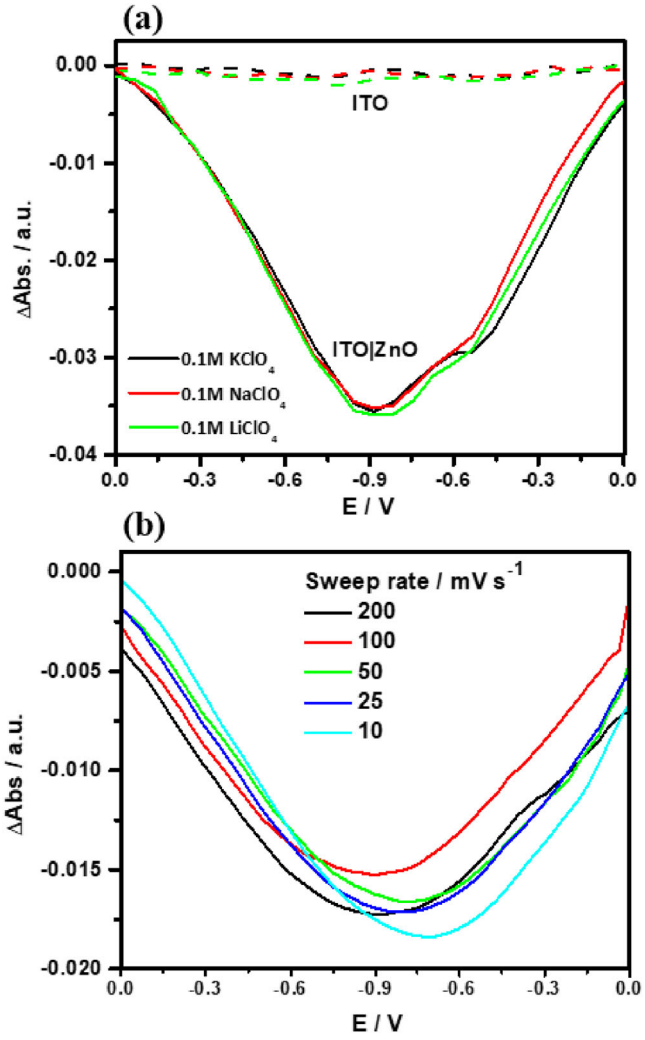

FIGURE 7 (A) Variation of *ΔAbs* at 370 nm with applied potential for sample *MP1* in different supporting electrolytes at 25 mV/s; (B) Variation of *ΔAbs* at 375 nm with applied potential for sample *MP4* at different sweep rates in 0.1 M $LiClO_4$

potential was recorded alongside with *ΔAbs*. The potential values are related to the accumulated electrons in the conduction band given by charge injection. The results are displayed in Figure 8. At -0.9V, when the solution was purged with N_2 (black curves), the optical change was larger and a stationary state was attained in 2-3 s instead of 10 s in O_2 presence (red curves). Therefore, this simple experiment indicates that dissolved O_2 in the electrolyte, affects both, maximum *ΔAbs* value and the kinetics of the process.

When the applied potential was interrupted (current was set to 0 A) in the presence of dissolved O_2, the optical change was completely reversed in about 40 s as well as the cell potential. However, in O_2 absence, the absolute values for *ΔAbs* were decreased by about 15% in 10 s, until reaching a stationary value for times greater than hundreds of seconds. The cell potential exhibits the same behavior: when the potential was interrupted, it decreased and

RESEARCH ARTICLE
doi.org/10.1002/elsa.202100035

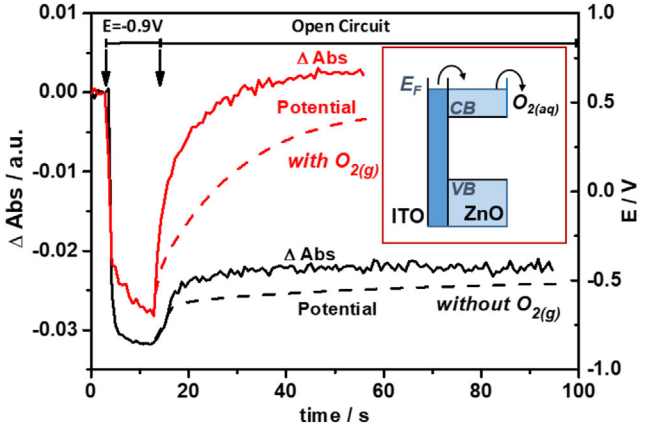

FIGURE 8 Variation of *ΔAbs* at 375 nm and cell potential with time for sample MP2 when applying a constant pulse of -0.9 V for 10 s and then letting the system relax at OCP, in the presence (red) and absence (black) of dissolved O_2. Inset: Band diagram of the spectroelectrochemical experiment containing O_2 dissolved in the aqueous solution. CB stands for Conduction Band, VB for Valence Band and EF for quasi-Fermi Energy

then maintained a constant negative value (-0.5 V) simultaneously with the optical change. This behavior clearly shows that the optical response can be directly associated with the electrochemical cell potential and electron concentration in the semiconductor conduction band. It has been reported that dissolved oxygen can react with electrons accumulated at the conduction band level in ZnO nanoparticles.[51,52]

When the electrode is polarized to negative overpotentials, such as -0.9 V, electrons are injected into the ZnO conduction band and the sample absorbance diminishes (Burstein-Moss effect). When the current is set to zero, electrons are no longer injected into the conduction band, so if the electrolyte solution is purged with N_2 (black curves, Figure 8) the O_2 concentration is very low, the injected electrons remain accumulated in the nanorods conduction band and *ΔAbs* reaches a plateau. On the other hand, when O_2 is present in the solution (red curves, Figure 8), after injecting the electrons into the conduction band they quickly react with O_2, depopulating the conduction band (see inset of Figure 8) and reversing the optical changes once the potential application was interrupted. These results exhibit that dissolved O_2 acts as an electron scavenger affecting the electrochemical Burstein-Moss shift development in time, magnitude, and also when the charge injection (charge accumulation under short-circuit conditions) is stopped. This is an interesting result showing that when O_2 concentration is very low, the conduction band of ZnO nanorods stays populated by electrochemical injected electrons for several seconds even when the potential is no longer applied.

3 | CONCLUSIONS

Wurtzite-type ZnO nanorods with different sizes and morphologies were successfully electrodeposited onto ITO from nitrate baths by varying the potential pulse program. When a single potential step is applied, large, hexagonal, and low surface density ZnO nanorods are deposited. If a multiple potential nucleation stage is included before growth, a much higher surface density of smaller ZnO nanorods is obtained. In both cases, the more negative the growth potential (or larger transfer charge), the smaller the ZnO nanorods; also, they are pointer and lose the hexagonal shape. This effect can be explained considering the presence of a dissolution process, mainly due to a chemical etching by HO^- ions.

The bleaching effect attained in the spectroelectrochemical experiments can be described as an electrochemical Burstein-Moss shift, and it is more notorious in samples with smaller ZnO nanorods, due to the larger availability of mid-gap states. These states can be populated or depopulated according to the externally applied potential.

Besides, it has been proven that optical changes are not affected by the electrolyte nature or concentration or the potentiodynamic sweep rate, only by ZnO morphology and dissolved oxygen content. Interestingly, the conduction band of ZnO nanorods stays populated by electrochemical charge injection for several seconds even when the potential is no longer applied and the cell is maintained at OCP in absence of dissolved O_2.

4 | EXPERIMENTAL SECTION

4.1 | Materials

ITO (indium tin oxide)-coated glasses (Delta Technologies, float glass cuvette slides 7 × 50 × 0.9 mm, Rs = 8 - 12 ohms), $Zn(NO_3)_2.6H_2O$ (Sigma-Aldrich), $NaNO_3$ (J.T. Baker), NaCl (J.T. Baker), $ZnCl_2$ (Sigma-Aldrich), $LiClO_4$ (Merk), LiCl (Anedra), $KClO_4$ (J.T. Baker), isopropanol, ethanol, acetone, and ultrapure deionized water (Millipore Q, 18.2 MΩ cm) were used in experiments. All chemicals were used as received without any further purification.

4.2 | Sample preparation

4.2.1 | ITO pretreatment

ITOs were pretreated by washing steps in an ultrasonic bath (Denimed bath, frequency 42 kHz) for 5 min each with the following sequence of solvents: isopropanol, acetone, ethanol, and deionized water. Afterward, an

RESEARCH ARTICLE
doi.org/10.1002/elsa.202100035
Chemistry Europe
European Chemical Societies Publishing

additional electrochemical cleaning step was performed to remove any impurities or organic material adsorbed on the ITO surface. This electrochemical cleaning consisted of a voltammetric cycling at 300 mV/s in a potential window from -1.0 V to 1.0 V versus $Ag|AgCl_{(s)}|KCl_{(aq,sat)}$ electrode in aqueous solution of 10 mM $LiClO_4$, using platinum as counter electrode. Once this cleaning step was completed, the ITO was rinsed with deionized water. The properly prepared ITO was used as working electrode during electrodeposition.

4.2.2 | ZnO electrodeposition

ZnO nanorods were potentiostatically electrodeposited (PGSTAT-101, Autolab EcoChemie) in a thermostated three-electrode cell with pre-treated ITO as working electrode and an $Au_{(s)}$ sheet and $Ag|AgCl_{(s)}|KCl_{(aq,sat)}$ as counter and references electrodes, respectively. The electrolytic solution was 1.0 mM $Zn(NO_3)_2.6H_2O$ + 0.5 M $NaNO_3$ and kept at a temperature of 80°C (Haake thermostat) during all the synthesis. The electrochemical cell was purged with N_2 for 10 min before starting the unstirred reaction and positive pressure was maintained throughout the electrodeposition.

Two sets of samples were prepared, according to the pulse potential program used: simple (samples named *SP-*) and multiple pulses (samples named *MP-*). In the first case, single potential pulses were applied from OCP (Open Circuit Potential) until potential values Ec between -0.8 V and -1.22 V until -200 mC/cm^2 (or the indicated value) of charge were transferred. In the second case, a seeding MPED stage is previously included. It involved a multiple potential program of 10 cycles, each one consisting of a pulse at -1.5 V for 1.0 s followed by a pulse at 0.16 V for 5.0 s. Once finished the seeding MPED stage, the growth of ZnO nanorods is carried out at a constant potential Ec until -50 mC/cm^2 of electric charge is transferred.

4.3 | Characterization and measurements

ZnO nanorods on ITO were characterized using SEM microscopy (secondary electrons) with a field emission scanning electron microscope (Supra FESEM, Sigma-Zeiss, LAMARX Laboratories, Córdoba, Argentina), operating at 4 kV. Raman spectra were acquired with a LABRAM-HR, Horiba Jobin-Yvon Raman microscope using a 514.5 nm Ar laser with an illuminated area of 1.0 μm^2 and a spectral resolution of 1.5 cm^{-1}. XRD patterns were acquired on an X-ray diffractometer Phillips X'pert Pro instrument equipped with a Pixcell 1D detector with 256 channels using Cu Ka (λ = 1.5418 Å) lamp operated at 40 kV, 40 mA at room temperature. Data were collected from 20θ to 70θ in continuous scan mode.

All electrochemical characterizations were conducted with a potentiostat/galvanostat (PGSTAT-101, Autolab EcoChemie) at room temperature. Photo and spectroelectrochemical measurements were carried out in a three-electrode electrochemical cell arranged inside a quartz cuvette. ZnO nanorods on ITO were front-side illuminated and placed as a working electrode. A platinum wire was the counter electrode and $Ag|AgCl|KCl_{(ac,sat)}$ was the reference electrode. 1.0 M $LiClO_4$ aqueous solutions (pH = 5.6) were used as electrolyte. Unless otherwise indicated, all solutions were previously purged with N_2 and positive pressure was maintained during the experiments. For photoelectrochemical experiments, a collimated Xe Lamp (Kratos LH-150/l 150 W) with a light spot of 0.2 cm^2 was used. Setup for spectroelectrochemical measurements involved the irradiation of the ZnO film with a collimated beam, via an optical fiber, from a Deuterium-Tungsten light source (Mini DT 1000 A, Analytical Instrument Systems Inc.) with a circular spot of 4 mm in diameter. The transmitted light was collected with an optical fiber and directed to a photodiode array spectrometer (Ocean Optics, HR2000+) covering a 200-1000 nm spectral range.

ACKNOWLEDGMENTS

V.B.L. acknowledges to Consejo Nacional de Investigaciones Científicas y Técnicas (CONICET) for the PhD fellowship granted. This work was financially supported by CONICET (PUE-2017 N° 22920170100092), Agencia Nacional de Promoción Científica y Tecnológica (ANPCyT-FONCyT, PICT-2018 N°2749) and by Secretaría de Ciencia y Tecnología, Universidad Nacional de Córdoba (SeCyT-UNC, CONSOLIDAR-2018 N° 33620180100118CB). Also, the authors want to acknowledge LAMARX laboratory for the scanning electron microscopy images.

DATA AVAILABILITY STATEMENT

Data included in the article supporting information, or on request.

ORCID

Cecilia I. Vázquez https://orcid.org/0000-0003-1852-1018
Victoria Benavente Llorente https://orcid.org/0000-0002-9830-7275
Franco M. Zanotto https://orcid.org/0000-0002-1459-5688

REFERENCES

1. C. B. Ong, L. Y. Ng, A. W. Mohammad, *Renew. Sustain. Energy Rev.* **2018**, *81*, 536.
2. E. J. Canto-Aguilar, M. Rodríguez-Pérez, R. García-Rodríguez, F. I. Lizama-Tzec, A. T. De Denko, F. E. Osterloh, G. Oskam, *Electrochim. Acta* **2017**, *258*, 396.
3. S. Qiao, J. Liu, G. Fu, K. Ren, Z. Li, S. Wang, C. Pan, *Nano Energy* **2018**, *49*, 508.
4. S. Cao, J. Zheng, J. Zhao, Z. Yang, C. Li, X. Guan, W. Yang, M. Shang, T. Wu, *ACS Appl. Mater. Interfaces* **2017**, *9*, 15605.
5. L. Zhou, H.-Y. Xiang, Y.-F. Zhu, Q.-D. Ou, Q.-K. Wang, J. Du, R. Hu, X.-B. Huang, J.-X. Tang, *ACS Appl. Mater. Interfaces* **2019**, *11*, 9251.
6. F. Rahman, *Opt. Eng.* **2019**, *58*, 1.
7. S. N. Sarangi, *J. Phys. D. Appl. Phys.* **2016**, *49*, 355103.
8. H. Wu, Z. Zheng, Y. Tang, N. M. Huang, R. Amal, H. N. Lim, Y. H. Ng, *Sustain. Mater. Technol.* **2018**, *18*, e00075.
9. C. Wang, L.-J. Wang, L. Zhang, R. Xi, H. Huang, S.-H. Zhang, G.-B. Pan, *J. Alloys Compd.* **2019**, *790*, 363.
10. C.-F. Liu, Y.-J. Lu, C.-C. Hu, *ACS Omega* **2018**, *3*, 3429.
11. D. Chen, A. Wang, M. A. Buntine, G. Jia, *ChemElectroChem* **2019**, *6*, 4709.
12. G. Rothenberger, D. Fitzmaurice, M. Graetzel, *J. Phys. Chem.* **1992**, *96*, 5983.
13. T. J. Jacobsson, T. Edvinsson, *J. Phys. Chem. C* **2013**, *117*, 5497.
14. D. Mandal, T. W. Hamann, *ACS Appl. Mater. Interfaces* **2016**, *8*, 419.
15. M. Kobielusz, K. Pilarczyk, E. Świętek, K. Szaciłowski, W. Macyk, *Catal. Today* **2018**, *309*, 35.
16. V. Benavente Llorente, C. I. Vázquez, M. A. Burgos, A. M. Baruzzi, R. A. Iglesias, *Electrochim. Acta* **2019**, *319*, 990.
17. E. Tosi, O. Marin, M. Tirado, D. Comedi, *Mater. Lett.* **2020**, *269*, 127658.
18. R. Nandi, S. S. Major, *Appl. Surf. Sci.* **2017**, *399*, 305.
19. X. Ma, J. Zhang, J. Lu, Z. Ye, *Appl. Surf. Sci.* **2010**, *257*, 1310.
20. M. A. Desai, V. Sharma, M. Prasad, S. Jadkar, G. D. Saratale, S. D. Sartale, *Int. J. Hydrogen Energy* **2020**, *45*, 5783.
21. J. S. Wellings, N. B. Chaure, S. N. Heavens, I. M. Dharmadasa, *Thin Solid Films* **2008**, *516*, 3893.
22. R. Salazar, C. Lévy-Clément, V. Ivanova, *Electrochim. Acta* **2012**, *78*, 547.
23. A. Henni, A. Merrouche, L. Telli, S. Walter, A. Azizi, N. Fenineche, *Mater. Sci. Semicond. Process.* **2015**, *40*, 585.
24. S. Sun, S. Jiao, K. Zhang, D. Wang, S. Gao, H. Li, J. Wang, Q. Yu, F. Guo, L. Zhao, *J. Cryst. Growth* **2012**, *359*, 15.
25. C. V. Manzano, D. Alegre, O. Caballero-Calero, B. Alén, M. S. Martín-González, *J. Appl. Phys.* **2011**, *110*, 043538, https://doi.org/10.1063/1.3622627
26. M. Stumpp, T. H. Q. Nguyen, C. Lupo, D. Schlettwein, *Electrochim. Acta* **2015**, *169*, 367.
27. M. Lakhdari, F. Habelhames, B. Nessark, M. Girtan, H. Derbal-Habak, Y. Bonnassieux, D. Tondelier, J. M. Nunzi, *Eur. Phys. J. Appl. Phys.* **2018**, 84.
28. N. Kıcır, T. Tüken, O. Erken, C. Gumus, Y. Ufuktepe, *Appl. Surf. Sci.* **2016**, *377*, 191.
29. M. Skompska, K. Zarębska, *Electrochim. Acta* **2014**, *127*, 467.
30. Z. Liu, L. E, J. Ya, Y. Xin, *Appl. Surf. Sci.* **2009**, *255*, 6415.
31. J. Jean, S. Chang, P. R. Brown, J. J. Cheng, P. H. Rekemeyer, M. G. Bawendi, S. Gradečak, V. Bulović, *Adv. Mater.* **2013**, *25*, 2790.
32. C. Te Hsieh, S. Y. Yang, J. Y. Lin, *Thin Solid Films* **2010**, *518*, 4884.
33. M. R. Khajavi, D. J. Blackwood, G. Cabanero, R. Tena-Zaera, *Electrochim. Acta* **2012**, *69*, 181.
34. S. Wei, J. Lian, X. Chen, Q. Jiang, *Appl. Surf. Sci.* **2008**, *254*, 6605.
35. Z. Liu, J. Ya, L. E, *J. Solid State Electrochem.* **2010**, *14*, 957.
36. A. Ait, L. Atourki, M. Ouafi, K. Abouabassi, A. Elfanaoui, A. Ihlal, K. Bouabid, *Solid State Sci.* **2020**, *104*, 106207.
37. C. V. Manzano, O. Caballero-Calero, S. Hormeño, M. Penedo, M. Luna, M. S. Martín-González, *J. Phys. Chem. C* **2013**, *117*, 1502.
38. J. Qiu, M. Guo, Y. Feng, X. Wang, *Electrochim. Acta* **2011**, *56*, 5776.
39. B. N. G. Trejo, R. Ortega, B. Y. Meas, V. P. Ozil, E. Chainet, *J. Electrochem. Soc.* **1998**, *145*, 4090.
40. T. Yoshida, D. Komatsu, N. Shimokawa, H. Minoura, *Thin Solid Films* **2004**, *451–452*, 166.
41. D. R. Lide, *CRC Handbook of Chemistry and Physics: A Ready-Reference Book of Chemical and Physical Data*, CRC Press **1992**.
42. C. I. Vázquez, G. I. Lacconi, *J. Electroanal. Chem.* **2013**, *691*, 42.
43. R. Zhang, P. G. Yin, N. Wang, L. Guo, *Solid State Sci.* **2009**, *11*, 865.
44. P. Sharma, J.-W. Jang, J. S. Lee, *ChemCatChem* **2019**, *11*, 157.
45. L. Gerbino, C. I. Vázquez, A. M. Baruzzi, R. A. Iglesias, *Electrochim. Acta* **2014**, *138*, 464.
46. L. M. Peter, *J. Solid State Electrochem.* **2013**, *17*, 315.
47. P. V. Kamat, N. M. Dimitrijevic, A. J. Nozik, *J. Phys. Chem.* **1989**, *93*, 2873.
48. I. Mora-Seró, F. Fabregat-Santiago, B. Denier, J. Bisquert, R. Tena-Zaera, J. Elias, C. Lévy-Clément, *Appl. Phys. Lett.* **2006**, *89*, 1.
49. C. J. Dahlman, Y. Tan, M. A. Marcus, D. J. Milliron, *J. Am. Chem. Soc.* **2015**, *137*, 9160.
50. S. C. Boehme, H. Wang, L. D. A. Siebbeles, D. Vanmaekelbergh, A. J. Houtepen, *ACS Nano* **2013**, *7*, 2500.
51. J. A. Faucheaux, P. K. Jain, *J. Phys. Chem. Lett.* **2013**, *4*, 3024.
52. T. Berger, J. A. Anta, V. Morales-Flórez, *J. Phys. Chem. C* **2012**, *116*, 11444.

SUPPORTING INFORMATION

Additional supporting information may be found online in the Supporting Information section at the end of the article.

How to cite this article: C. I. Vázquez, V. B. Llorente, F. M. Zanotto, A. M. Baruzzi, R. A. Iglesias, *Electrochem Sci Adv* **2021**;e2100035. https://doi.org/10.1002/elsa.2100035.